Aalto University

OPEN ACCESS

This is an electronic reprint of the original article.
This reprint may differ from the original in pagination and typographic detail.

Korhonen, E.; Tuomisto, F.; Bierwagen, O.; Speck, J.S.; Galazka, Z.

Compensating vacancy defects in Sn- and Mg-doped In2O3

Published in:
Physical Review B

DOI:
10.1103/PhysRevB.90.245307

Published: 01/12/2014

Document Version
Publisher's PDF, also known as Version of record

Please cite the original version:
Korhonen, E., Tuomisto, F., Bierwagen, O., Speck, J. S., & Galazka, Z. (2014). Compensating vacancy defects in Sn- and Mg-doped In_2O_3. *Physical Review B*, *90*(24), 1-7. [245307]. https://doi.org/10.1103/PhysRevB.90.245307

This material is protected by copyright and other intellectual property rights, and duplication or sale of all or part of any of the repository collections is not permitted, except that material may be duplicated by you for your research use or educational purposes in electronic or print form. You must obtain permission for any other use. Electronic or print copies may not be offered, whether for sale or otherwise to anyone who is not an authorised user.

Compensating vacancy defects in Sn- and Mg-doped In_2O_3

E. Korhonen,[1] F. Tuomisto,[1] O. Bierwagen,[2,3] J. S. Speck,[2] and Z. Galazka[4]
[1] *Department of Applied Physics, Aalto University, FI-00076 Aalto, Finland*
[2] *Materials Department, University of California, Santa Barbara, 93106 California, USA*
[3] *Paul-Drude-Institut für Festkörperelektronik, Hausvogteiplatz 5–7, DE-10117 Berlin, Germany*
[4] *Leibniz Institute for Crystal Growth, DE-12489 Berlin, Germany*
(Received 27 June 2014; revised manuscript received 9 December 2014; published 29 December 2014)

MBE-grown Sn- and Mg-doped epitaxial In_2O_3 thin-film samples with varying doping concentrations have been measured using positron Doppler spectroscopy and compared to a bulk crystal reference. Samples were subjected to oxygen or vacuum annealing and the effect on vacancy type defects was studied. Results indicate that after oxygen annealing the samples are dominated by cation vacancies, the concentration of which changes with the amount of doping. In highly Sn-doped In_2O_3, however, these vacancies are not the main compensating acceptor. Vacuum annealing increases the size of vacancies in all samples, possibly by clustering them with oxygen vacancies.

DOI: 10.1103/PhysRevB.90.245307 PACS number(s): 77.84.Bw, 61.72.jd, 78.70.Bj

I. INTRODUCTION

Transparent conducting oxides (TCOs), such as indium-tin-oxide (In_2O_3:Sn, ITO), antimony-doped tin oxide (SnO_2:Sb, ATO), tin-doped gallium oxide (β-Ga_2O_3:Sn), and Al-doped zinc oxide (ZnO:Al, AZO), combine high electrical conductivity due to high donor doping with optical transparency due to the wide band gap. These properties make TCOs an important material category for optoelectronic applications with the most common use as transparent contacts on products such as liquid crystal displays and solar cells [1]. ITO is the most used TCO since it can be grown into thin films with resistivity as low as 1×10^{-4} Ω cm. Indium is not as earth abundant as zinc or tin so a search for a substitute for ITO is under way. So far, none of the possible substitutes have been able to reach both the electrical properties and manufacturing practicality of ITO [2].

Without the excessive doping, these TCOs are called transparent semiconducting oxides (TSOs), being wide band-gap semiconductors (In_2O_3, SnO_2, β-Ga_2O_3, and ZnO) that are insulating in their perfectly stoichiometric form. Recently, In_2O_3 and similar TSOs have been discovered as active device materials for transparent (display) electronics, UV detectors, and power electronics [3].

The most common TSOs are n-type conductive in their undoped form—they are unintentionally doped (uid). The exact nature of the unintentional donors is not known, but calculations and experiments point to the intrinsic donor defect oxygen vacancies (V_O) and cation interstitials (In_i in In_2O_3) [3–6], or hydrogen as a source of donors [3,6,7]. Consequently, the electronic properties of the film are heavily dependent on the growth parameters such as oxygen partial pressure and temperature.

To increase the conductivity beyond the uid level, extrinsic n-type dopants are usually added to TSOs. For In_2O_3 the most common donor is Sn [3]. At Sn concentrations of 10^{21} cm^{-3} (and similar electron concentration) the TSO In_2O_3 turns into the TCO ITO. Oxygen-rich growth conditions or post-growth annealing of ITO films in oxygen-containing environments, however, significantly reduces the electron concentration [8,9], suggesting strong compensation of the Sn donors by the intrinsic acceptor defect indium vacancies (V_{In}) or oxygen interstitials (O_i) [4,5].

A significant current problem is that p doping is difficult to the point of being impractical. For example, acceptor doping of In_2O_3 by Mg [10] resulted in n-type conductive films after growth or annealing in vacuum, and annealing in oxygen resulted in semi-insulating films but no p-type conductivity. The n-type conductivity is clearly related to overcompensation—likely by V_O. The absence of p-type conductivity even after annealing in oxygen could be related to exact compensation, or Mg being a deep acceptor, or polaronic hole localization [11,12].

For use as a true semiconductor, greater understanding and control on material properties and doping is required. All experimental findings suggest intrinsic point defects to play a major role in influencing the conductivity of In_2O_3. Recent calculations of their formation energy using state-of-the art *ab initio* theory [4,5,7,13–15] agree on a reduced formation energy—corresponding to increased equilibrium concentration—of the donorlike defects (V_O, In_i) and acceptorlike defects (V_{In} and O_i) for low and high Fermi levels, respectively, indicating the tendency of these point defects to compensate intentional doping that decrease (acceptor) and increase (donor) the Fermi level, respectively. In addition, these calculations indicate a reduced formation energy of the donorlike and acceptorlike defects for indium-rich (oxygen poor) and oxygen-rich (indium poor) conditions, respectively. Both these tendencies qualitatively agree with the above-mentioned experimental finding on compensation of Sn and Mg doping.

While theory agrees on V_O being a more likely donor than In_i [4,5], a disagreement on the dominant compensating acceptor remains: Without the use of hybrid functionals, V_{In} were calculated to have lower formation energy than O_i for a Fermi level high in the conduction band under In-rich conditions and even for a lower Fermi level under O-rich conditions [4,5]. Using hybrid functionals, in contrast, O_i was calculated to have the lower formation energy also under O-rich conditions up to band filling of 1 eV (corresponding to $\approx 10^{21}$ cm^{-3} electrons [16]) [13].

Despite these theoretical suggestions on the possible role of V_{In} as compensating acceptor in ITO and lower-doped In_2O_3,

 ©2014 American Physical Society

their experimental investigation is still missing. So far, theoretical analysis and transport investigations of ITO annealed in oxidizing and reducing environments in conjunction with structural investigations have only addressed the compensating role of O_i by formation of neutral clusters with two nearby Sn donors [8,17,18].

Positron annihilation spectroscopy is a powerful method for studying vacancy defects in semiconductors [19]. In this work we use positron annihilation spectroscopy to identify and quantify the acceptor type vacancy defects V_{In} in Sn- and Mg-doped In_2O_3. Through comparison with electrical characterization, we propose a compensation mechanism based on intrinsic defects in In_2O_3.

II. SAMPLE PREPARATION AND EXPERIMENTAL TECHNIQUES

A. Sample preparation

1. *Thin-film* In_2O_3

A series of high quality single crystalline thin-film Sn- and Mg-doped In_2O_3 samples was prepared using plasma-assisted molecular beam epitaxy (PA-MBE) on yttria-stabilized zirconia (YSZ) substrates [9,10]. An undoped thin-film sample was included for comparison. Basic sample information can be found in Table I. While doping by the donor Sn is expected to induce the formation of acceptor-type compensating defects, doping by the acceptor Mg doping is rather promoting donor-type compensating defects. During growth, the temperature of the YSZ substrate was between 630 °C and 650 °C. The dopant concentration was measured using secondary ion mass spectrometry. The thickness of the total In_2O_3 layer was determined with cross-sectional scanning electron microscopy. Temperature-dependent Hall effect measurement was used for determining charge carrier properties. X-ray diffraction scans show single phase material. After growth, different pieces of the grown samples were thermally annealed to influence the intrinsic defect concentration. To promote the formation of the acceptor-type defects (O_i and V_{In}) and inhibit that of donor-type defects (V_O and In_i), oxygen annealing was performed at 750 °C with 1 atm O_2 for 30 s in a rapid thermal annealing setup. Conversely, vacuum annealing was performed at 700 °C for 10 min with total pressure below 10^{-6} Torr in a vacuum chamber, aiming at increasing the concentration of donor-type defects V_O and In_i and reducing that of acceptor-type defects O_i and V_{In}. Both these annealings have been found to significantly change the electron concentration in our films [9,10].

TABLE I. Thin-film sample information. Listed are the thicknesses, dopant concentrations, and electron concentrations after both annealings. Sample No. 7 was grown without intentional doping. * was measured in the as-grown sample.

Sample number	d nm	[Sn] cm^{-3}	[Mg] cm^{-3}	n_e (O_2) cm^{-3}	n_e (vac.) cm^{-3}
No. 1	618	8.5×10^{20}	–	2.3×10^{20}	1.4×10^{21}
No. 2	396	8.2×10^{19}	–	3.9×10^{19}	4.3×10^{19}
No. 3	518	4.7×10^{18}	–	3.0×10^{18}	$5.0 \times 10^{18*}$
No. 4	419	–	8.8×10^{19}	≈ 0	$\approx 1 \times 10^{18}$
No. 5	418	–	3.3×10^{19}	≈ 0	$\approx 1 \times 10^{18}$
No. 6	422	–	2.1×10^{18}	$\approx 1 \times 10^{17}$	$\approx 1 \times 10^{18}$
No. 7	776	–	–	1.4×10^{17}	1.0×10^{18}

2. *Bulk* In_2O_3 *crystal*

Pure (i.e., undoped) bulk In_2O_3 crystals were grown from the melt by a novel crystal growth technique under the name levitation-assisted self-seeding crystal growth method, as described in Refs. [20,21]. Then the bulk crystals were annealed in an oxidizing atmosphere at 1000 °C for 40 h to oxidize In nanoparticles formed during the growth and therefore to improve the optical transmittance [22,23]. The samples were both sides epi-polished. They were yellowish and had a very steep absorption edge originating at 440 nm [22]. The free electron concentration in these crystals is 2–5 $\times 10^{17}$ cm^{-3} and mobility 160–190 cm^2/Vs [21,22].

B. Positron annihilation experiments

The samples were studied using positron annihilation spectroscopy, a versatile tool for studying vacancy-type defects [19]. The method is based on implanting the target with positrons and detecting the 511-keV gamma quanta produced by the subsequent electron-positron annihilation. Since positrons are repelled by the positive charge of the atom cores, neutral and negatively charged vacancy defects usually act as positron traps. In a vacancy, both the electron density and average electron momentum are reduced compared to the lattice. This means that a positron localized to a vacancy tends to live longer than a delocalized positron.

For a lifetime measurement, a small amount of β^+-active material is wrapped inside thin aluminium foil to form a positron source. Sample pieces are attached on both sides of the source and the source-sample "sandwich" is then placed between two scintillator detectors. The system is optimized for time resolution at the cost of energy resolution.

The lifetime of an individual positron can be observed by measuring the time difference between the positron emission and annihilation signals. Typically the positrons are obtained from Na-22, which also emits a 1.27-MeV gamma quantum immediately after the decay. The gamma quanta are detected by scintillator detectors. The voltage signals are digitized and fed to a PC, where signal analysis is performed by fitting a cubic spline to the rising edge of the pulse. In this fashion, the pulses can be timed with subnanosecond accuracy. The limiting factor for the time resolution are the detectors, especially the plastic scintillator crystals. Positron lifetime is typically only measured in bulk samples, since the positrons obtained from Na-22 have an exponential depth distribution extending to about 200 μm in In_2O_3 in the sample.

By collecting a large number of counts (over 10^6) a lifetime spectrum is formed, from which the annihilation time constants (called lifetimes) can be deduced. The lifetime value of a component is mostly dependent on the size of the corresponding defect; usually the lifetimes are of the order of 150–300 ps in semiconductors. The intensities of the components are dependent on the concentrations and trapping coefficients of the different defect types. The final lifetime distribution is a sum of exponentially decaying

components, from which the lifetimes can be resolved by fitting. If the concentration of vacancies which trap positrons is sufficiently low, only a single component is seen [19]. A single lifetime component can also be observed in the case of saturation trapping of positrons to a high defect concentration ($>10^{19}$ cm^{-3}).

When studying thin films, a monoenergetic slow positron beam is required to control the implantation energy and hence the depth distribution of positrons. Depending on the positron kinetic energy, the depth probed may be tuned from the surface to roughly 2 μm. The width of the implantation distribution is similar to the mean implantation depth and in addition, the positron diffusion length in solids after thermalization is in the 100-nm range, although heavily dependent on the concentration of vacancies. Due to these factors, the annihilation signal is received from a significant depth slice.

In a traditional positron beam, instead of measuring the positron lifetime, the Doppler broadening of the 511-keV positron-electron annihilation radiation peak is detected. This broadening is caused mainly by the momentum distribution of the annihilating electrons. One high-purity Ge detector with an energy resolution of 1.3 keV [full width at half maximum (FWHM)] at 511 keV was used for measuring the spectrum. To describe the spectrum in a brief fashion, two parameters S and W are typically used. The low momentum parameter S is the fraction of counts in the central region of the peak, while W corresponds to the fraction of counts in the wing areas on both sides of the peak. The W parameter is more sensitive to highly localized core electrons. The integration windows are set symmetrically around the peak. In this work, annihilation events corresponding to the longitudinal (detector axis) momentum component of the electron-positron pair in the range of -0.4–0.4 a.u. define the S parameter. The W windows were set as ±1.6–4.0 a.u. For sufficient statistics, approximately half a million counts were collected for each measurement point.

Typically, an increase in the value of S indicates an increase in open volume defects in the depth being probed, mainly due to the reduced overlap of the positron wave function with core electron wave functions when the positron is trapped in a vacancy. The value of W is more dependent on the type of atoms surrounding the annihilation site.

III. RESULTS

A. Lifetime spectroscopy

The high crystal quality bulk In_2O_3 sample was used as a reference for both lifetime and Doppler broadening measurements. A total of 3 million counts was collected for the positron lifetime spectrum and the FWHM of the spectrometer Gaussian resolution function was 250 ps.

The measured positron lifetime spectrum for the bulk crystal and the model function fit result are illustrated in Fig. 1. In the figure, lifetime components arising from annihilations in the positron source material have been subtracted from the spectrum with intensity 4.0% for the 235-ps Al-foil component, 3.0% for 400-ps Na-22 salt component, and 0.18% for the 1500-ps positronium component. The intensity of the 235-ps component was calculated using a formula from

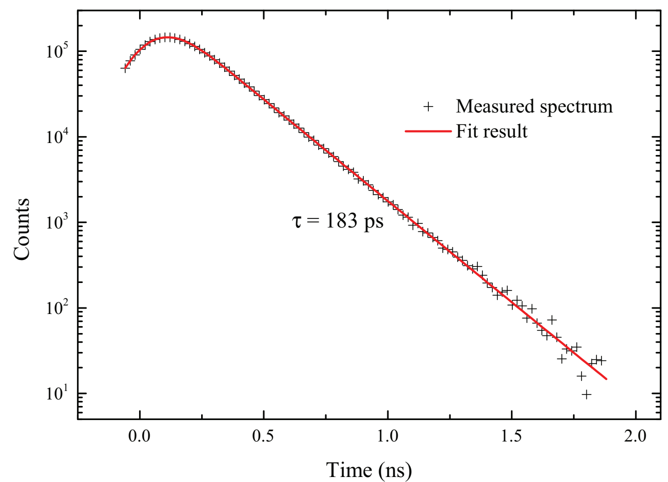

FIG. 1. (Color online) Lifetime spectrum of the bulk crystal sample after subtraction of source components and background. On a logarithmic scale the spectrum forms a line, indicating that only a single annihilation state is seen by positrons.

Bertolaccini and Zappa [24]; it was not fitted. This reduces the chance of this component shadowing a sample related lifetime. The spectrum arising from annihilations in the sample fits very well to a single line, indicating that only one exponential component with $\tau_0 = 183$ ps is detected. Typically, in related materials the free positron lifetime is in the 170- to 180-ps range: 175–181 ps in SnO_2 [25,26], 170 ps in ZnO [27], and 184 ps in InN [28]. Cation vacancy lifetimes in these kinds of crystals are significantly higher than the bulk, usually by 40–80 ps. The observed lifetime is hence likely the positron lifetime in the In_2O_3 lattice, which means that the cation vacancy concentration in the sample is below the detection limit of 10^{16} cm^{-3}. Although a single lifetime can also be explained by saturation trapping to a vacancy defect (requiring a high $>10^{19}$ cm^{-3} vacancy concentration) this is unlikely, since in the Doppler broadening results (Fig. 4) the bulk sample is shown to be grouped with the samples with the smallest vacancy concentrations.

B. Doppler broadening

Figures 2 and 3 show the low momentum parameter S as a function of implantation energy for the Sn- and Mg-doped film samples. The corresponding mean implantation depth is marked on the top axis. Figure 2 also includes a plot of positron depth distributions for a few implantation energies to illustrate the shape of the depth profile. As can be seen, the width of the positron depth distribution is approximately equal to the mean implantation depth. At high energies the values of S and W should change more smoothly than at low energies. This also explains why the substrate is partially seen already at 10 keV for the thinnest samples.

Most of the samples give results with similar forms. Three regions can be distinguished: surface, In_2O_3 film, and substrate. At low energies ($E < 3$ keV), the effect of surface annihilations dominates due to the diffusion of thermalized positrons (indicating a positron diffusion length of less than 30 nm) and gives a quickly changing S as the energy increases.

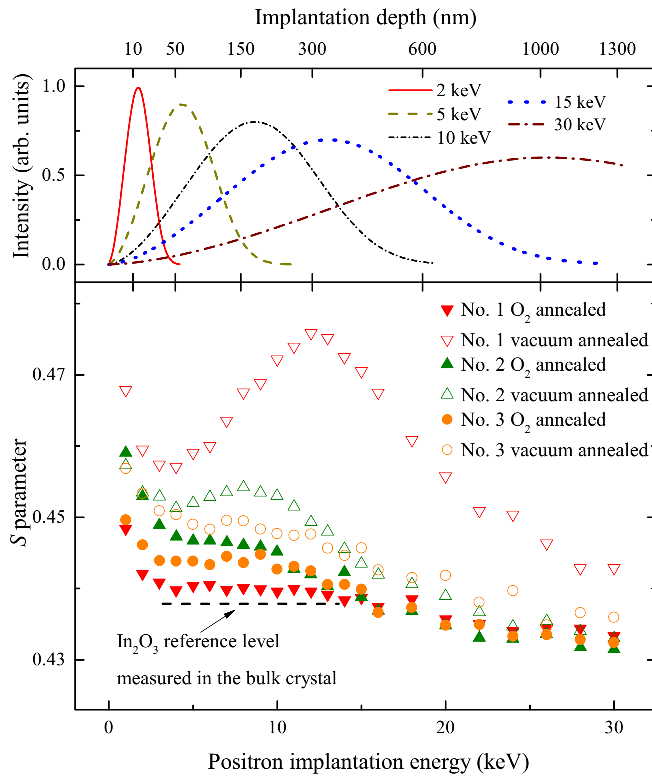

FIG. 2. (Color online) S parameter as a function of implantation energy for the Sn-doped samples after different annealings. The S value obtained by averaging the In_2O_3 bulk sample measurement results at high energies is marked with a dashed line. In the upper figure, positron implantation profiles for selected energies are drawn to better illustrate the effective probing depth as a function of energy. The depth values on the upper horizontal axis correspond to the mean implantation depths caused by the matching implantation energy values on the lower horizontal axis. The implantation profiles are not in correct height scale. The purpose of the upper figure is to illustrate how the measured values are averages from the signals from different depths.

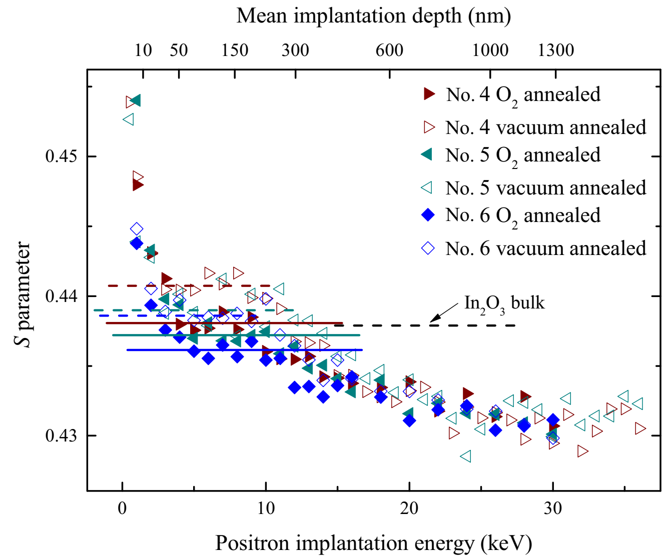

FIG. 3. (Color online) S as a function of positron implantation energy for the Mg-doped samples with different annealings. Horizontal lines illustrate the averaged layer values. The lines have the same color as the sample marker with dashed and full lines indicating vacuum and O_2 annealing, respectively. Generally, the differences between the samples are small compared to the Sn-doped samples.

For middle energies ($E \in [5,10]$ keV) the In_2O_3 film typically gives a steady value. At high energies ($E > 15$ keV) the substrate signal becomes visible and eventually dominates the S value.

As can be seen in Fig. 2, the oxygen annealed samples resemble each other from a positron perspective. The layer S values do not seem to correlate with doping concentration. The interface between In_2O_3 and the substrate is not visible and S transitions smoothly from the layer to the substrate. The S is still higher than the In_2O_3 bulk value, which indicates that some vacancies with concentrations greater than 10^{16} cm^{-3} are detected.

The vacuum annealed samples on the other hand show interesting features. They have a higher S value in the In_2O_3 layer compared to the O_2 annealed samples. Also, the doping concentration order matches the layer S ordering. For samples No. 1 and No. 2 the value of S increases between the layer and the substrate, indicating that a distinguishable region forms at the interface. The peaks in S are not at the same positions for the two samples since the thicknesses of the In_2O_3 layers differ by 200 nm. Also, the locations of the peaks (12 and 8 keV) correspond to roughly half of the layer thicknesses. According to the depth distributions in Fig. 2, at these energies only a minor amount of positrons are implanted to the substrate. For sample No. 2, it seems the interface effect is mostly limited to the energy range matching the In_2O_3 layer with the substrate remaining relatively unaffected. In the case of sample No. 1, due to the high interface value of S and the width of the positron depth distribution at high energies, the effect is seen also at much higher energies. Generally, it seems that the strength of the interface effect correlates with the doping concentration so that for sample No. 3 the interface is no longer clearly visible.

For the Mg-doped samples the measurement results are quite uniform. The absolute scale for S-parameter values in the In_2O_3 layers is only roughly 0.005 wide compared to 0.02 for the Sn-doped samples. This is consistent with the fact that the differences between dopant concentrations within each sample group are different: In the Sn-doped case the ratio of highest dopant concentration to the lowest is 180, while for the Mg-doped case the ratio is 40.

Distinguishing the Mg-doped samples from each other is difficult. Still, it can be seen that on average the oxygen annealed samples have lower S than the vacuum annealed ones. There is no clear interface effect on the vacuum annealed samples. Still, the doping seems to have an effect as the layer S values increase slightly with the doping in both the oxygen and vacuum annealed cases.

IV. DISCUSSION

A. S-W plots

To better illustrate the differences of annihilation parameters in the In_2O_3 layer between different samples two S-W

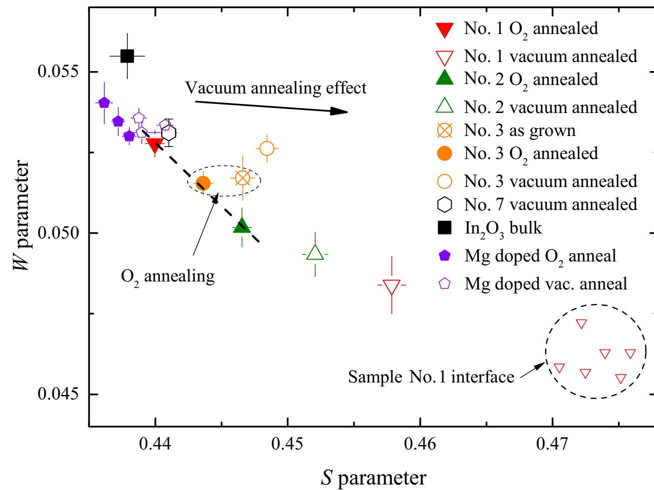

FIG. 4. (Color online) S-W plot for the Sn-doped samples (No. 1–No. 3). Each sample is described by one point. In addition, a point for the In_2O_3 bulk sample, the undoped sample No. 7 and an area for the interface in sample No. 1 are illustrated.

plots are shown in Figs. 4 and 5. For most samples, only one point is drawn. These layer (S,W)-value pairs are determined by taking the corresponding average from the energy range 3–12 keV, although the exact range was varied from sample to sample to take into account the different layer thicknesses and to avoid averaging over extended interface effects. Also, a data point for the bulk sample is shown. The (S,W) value for this sample in the figures was calculated as an average from the energy range 20–36 keV. The error bars indicate the statistical deviation within the selected energy range.

Figure 4 shows the difference between the oxygen and vacuum annealed layers for the Sn-doped samples. Vacuum annealing causes a general shift to higher S indicating an increase in detected open volume. For most samples W correspondingly decreases. The total shift is greatest for sample No. 1. It is notable that the transition to the interface (S,W) values for this sample is similar in magnitude to the annealing effect. The three oxygen annealed samples fall on a line together with the Mg-doped samples, which usually indicates that only one type of defect is seen by positrons. This does not apply for the vacuum annealed samples.

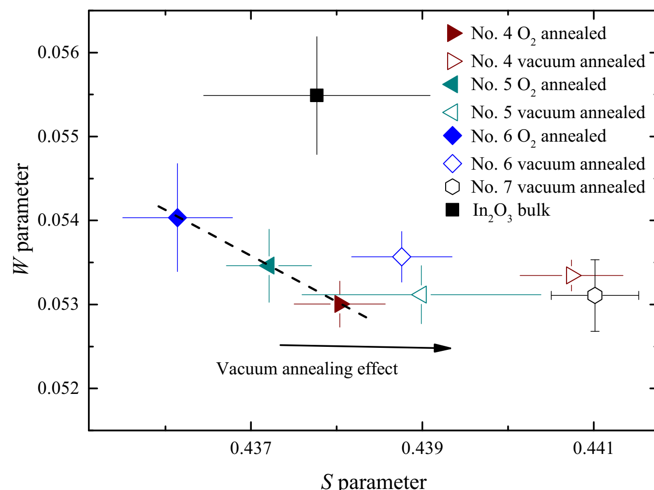

FIG. 5. (Color online) S-W plot for the Mg-doped samples (No. 4–No. 6) and the undoped sample No. 7. Each sample is described by one point. As the differences between samples are small, the error bars on the points become significant in comparison.

The as-grown sample No. 3 is located between its O_2-annealed and vacuum-annealed versions. This sample may be considered slightly vacuum annealed, since the samples were grown in a low pressure environment at temperatures only 50 °C lower than the actual annealing. Accordingly, the (S,W) point moves to lower S during O_2 annealing as oxygen returns to the sample.

With the Mg-doped samples the differences are less pronounced. Figure 5 is a zoomed-in view to the upper left corner of Fig. 4. Similarly to the Sn-doped samples, vacuum-annealed samples have higher S and typically lower W than their O_2-annealed counterparts. Again, the oxygen-annealed samples fall on a line.

B. Defect identification and electrical compensation

1. *Sn-doped* In_2O_3

After oxygen annealing, the Sn-doped samples form a line (Fig. 4), indicating a single vacancy type. Comparing the (S,W) values of the three points with that of the bulk sample one can estimate that $S_{\text{defect}} \geqslant 1.02 \times S_{\text{bulk}}$ and $W_{\text{defect}} \leqslant 0.90 \times W_{\text{bulk}}$. It is worth noting that Sn is not the primary factor in determining the vacancy defect concentration as the locations of the samples on the line in Fig. 4 do not follow the Sn concentration.

Small anion vacancies, even if clustered together, do not trap positrons in these kinds of strongly cation-anion radius-mismatched compounds [29]. Hence, these defects must be related to indium vacancies (V_{In}) [14]. In the following, we show that the V_{In}-related defects detected with positrons are most probably complexes involving both V_{In} and V_{O}.

After vacuum annealing a significant shift in the layer values is seen. Compared to the bulk value the new span is $S_{\text{defect}} \geqslant 1.05 \times S_{\text{bulk}}$ and $W_{\text{defect}} \leqslant 0.87 \times W_{\text{bulk}}$. Although the relative change is similar for both S and W, the horizontal move is more consistent. In any case, the three points are no longer on the same line as is with the O_2-annealed samples. This indicates that a different type of defect is being detected, either replacing or augmenting the ones in the O_2-annealed samples. The S parameter is mainly dependent on the valence electron density seen by positrons (in contrast to core electrons), which in turn correlates with vacancy size. A common increase in S as seen by the vacuum annealing effect can be explained by adding more vacancies next to indium vacancies. Since vacuum annealing is assumed to remove oxygen from the samples, the obvious interpretation is that more V_{O} is added to the indium vacancies. This is consistent with a general increase in oxygen vacancy concentration throughout the In_2O_3 layer, which in turn would explain the increase in conduction electron concentration compared to the O_2-annealed samples.

A similar effect is seen in InN [29]. Rauch *et al.* find that isolated V_{N} do not trap positrons while V_{In} do. A horizontal shift in the S-W plane is seen when V_{N} is added next to V_{In},

the size of the shift dependent on the number of nitrogen vacancies added. This effect is due to the positron annihilation rate with N 2p electrons decreasing when N adjacent to the V_{In} is removed. A similar effect is expected for O 2p electrons. In fact, recent computational results [30] for vacancy complexes in ZnO predict this: Adding one or more V_O next to V_{Zn} moves the (S,W) point to the right, and further adding H in place of V_O moves the result back towards the V_{Zn} point.

According to the S-W data, the O_2-annealed samples contain only one type of trapping defect. In this case the vacancy concentration of the samples can be estimated with

$$c_D = N_{at}\frac{\lambda_B}{\mu_D}\frac{S - S_B}{S_D - S}, \quad (1)$$

where N_{at} is the atom density, λ_B is the annihilation rate in the host lattice, μ_D is the defect-specific trapping coefficient, and finally S_B and S_D are the S values of the bulk and defect states. $\lambda_B = 5.5 \times 10^9$ s^{-1} is known from the lifetime measurement. For μ_D, the value 3×10^{15} s^{-1} is typical of cation-type defects in compound semiconductors [19] and is used here. $S_B = 0.438$ as was measured. The value of S_D is on the line formed by the O_2-annealed samples in Fig. 4 but its exact location is unknown. It can be estimated from InN, where the indium vacancy has $S_D = (1.04\text{–}1.05) \times S_B$. In the case of In_2O_3, this value corresponds to $S_D = 0.455\text{–}0.460$. Using the measured values for S, the defect concentrations of samples No. 1–No. 3 can be resolved to be in the ranges $1.5\text{–}1.9 \times 10^{16}$ cm^{-3} for No. 1, $0.9\text{–}1.4 \times 10^{17}$ cm^{-3} for No. 2, and $5.0\text{–}6.9 \times 10^{16}$ cm^{-3} for No. 3.

The dopant and electron concentrations listed in Table I for the oxygen-annealed samples No. 1 to No. 3 do not match, indicating compensating acceptors. If we assume that the only donor is the Sn dopant (each supplying one conduction electron), the concentrations of the acceptors for the samples must be $N_A = [n] - N_D$, which leads to values 6.2×10^{20}, 4.3×10^{19}, and 1.7×10^{18} cm^{-3} for No. 1, No. 2, and No. 3, respectively. Comparing these numbers with the vacancy concentrations estimated above, it is clear that neither the magnitudes nor the trends match between vacancies and acceptors. This indicates that the dominant compensating acceptor is not the V_{In} or a V_{In}-related defect. A good candidate is an interstitial defect, for example, the O_i, which has been predicted to cluster around Sn dopants [5,8,17]. A negatively charged ion, such as an ionized O_i, can act as a shallow positron trap. In a Doppler spectrum the presence of shallow traps would be seen as the signal moving closer to the bulk (S,W) value, since a positron trapped to a shallow state is relatively delocalized. However, shallow traps are rarely visible in room temperature due to thermal detrapping so the presence of O_i can not be commented on based on these measurements.

In samples No. 1 and No. 2 the vacuum annealing also creates a significant vacancy concentration at the interface between the In_2O_3 and the YSZ. The amount of V_O surrounding the V_{In} seems to be higher near the interface than in the In_2O_3 layer, however, Eq. (1) cannot be used in this case since the type of vacancy is changing. The strength of this effect seems to correlate with dopant concentration: The higher the [Sn] is, the more pronounced is the difference between layer and interface S values and vacancy concentrations. A similar effect is seen in Si-doped InN on sapphire substrate [31], where the region near the interface has a markedly increased dislocation density and various point defects.

2. *Mg-doped* In_2O_3

The results for the Mg-doped samples show similar behavior as the Sn-doped samples, the changes are simply much smaller, in the sub-1% range compared to the bulk sample values. The oxygen-annealed samples once again form a line, which is a signal that only one type of positron trap exists. The least doped sample is now the leftmost one on the line in contrast to the Sn-doped case. After annealing in vacuum, the points move horizontally to larger S while the scale of W values stays mostly constant. As with the Sn-doped samples, the type of defect seems to change. The annealing effect is less evident than in the Sn-doped samples. The point for the undoped, vacuum annealed thin-film sample No. 7 is located near the Mg-doped samples. This is in line with the similarity in the free carrier concentrations between the Mg-doped and undoped samples.

After growth, all Mg-doped films were found to be n-type conductive with values comparable to undoped In_2O_3, which means the Mg was overcompensated by intrinsic defects [10]. Sample No. 5 received an exceptionally large amount of oxygen and was more resistive than the others. After annealing in oxygen, the resistivity of all samples increases, often by an order of magnitude. Annealing in vacuum turns the films back to n-type conductive. The conclusion is that annealing in oxygen removes donor-type oxygen vacancies from the films, with the remaining ones being balanced by Mg. Vacuum annealing removes the oxygen. This is in line with the positron data.

Although the samples never were p-type conductive, it can be assumed that Mg-doping lowers the Fermi energy, making sure that V_O is in its 2+ charge state and is even less visible to positrons than in the Sn-doped case. Also, the formation energy of V_{In} is higher in p-type material than in n type [13]. Hence, it is natural that the Mg-doped samples give S values that are close to the perfect lattice, as V_{In} should be rare, and Mg should substitute In. Thus, the vacancies are mostly limited to V_O, which are not seen. The vacuum annealing effect is similar as in the Sn-doped case, namely increasing the concentration of V_O, from which those that are near V_{In} are seen by positrons. The actual concentration of V_{In} does not change as much as with the Sn-doped samples as the Mg concentration changes.

Interestingly, the data points in Fig. 5 for the O_2-annealed Mg-doped samples are directly below or to the left of the point measured in the In_2O_3 bulk crystal. Two reasons thus far are possible: The bulk In_2O_3 is not as ideally defect free as interpreted from the lifetime experiments, or Mg_{In} creates a similar small positron trap as Li_{Zn} in ZnO, with very peculiar S and W parameters [32]. Further investigations are required to resolve this.

V. SUMMARY

Compensating vacancy defects (V_{In}, V_O) were investigated by positron annihilation spectroscopy in Sn-donor and Mg-acceptor doped In_2O_3 thin films, and in an unintentionally doped bulk In_2O_3 reference sample. The films were annealed

in oxygen or vacuum to alter the compensating defect concentration.

In both types of oxygen-annealed films only one type of vacancy, acceptor-type V_{In}, was detected by the positrons. The concentration of the V_{In} was higher in Sn-donor doped samples than in Mg-acceptor doped samples. In highly Sn-donor doped In_2O_3 (ITO), however, the V_{In} concentration was orders of magnitude lower than the compensating acceptor concentration (determined by the difference of the Sn-donor concentration and the significantly lower electron concentration) induced by the annealing. These findings support the picture of interstitial oxygen O_i and not V_{In} to be the main compensating acceptor in ITO [17]. Whether the lack of *p*-type conductivity and semi-insulating behavior in the Mg-doped samples was due to exact compensation by V_O cannot be concluded from our data because we cannot detect isolated V_O.

Annealing in vacuum changed the type of vacancies in all samples instead of only changing their concentration. The results suggest clustering of oxygen vacancies next to V_{In}. In all samples, the vacuum annealing also increased conduction electron concentration, consistent with adding donor type V_O to the samples (and, additionally removing compensating O_i in ITO). The *n* conductivity of the Mg-doped samples suggests overcompensation of the Mg by V_O.

The unintentionally doped bulk crystal sample was found to lack any vacancies detectable by positron annihilation. This is in line with the high formation energy of V_{In}, as in thin-film growth kinetic effects often create favorable conditions for vacancy formation even when thermodynamics does not support it [33].

ACKNOWLEDGMENT

This work was supported by the Academy of Finland.

[1] T. Minami, Thin Solid Films **516**, 5822 (2008).
[2] A. Kumar and C. Zhou, ACS Nano **4**, 11 (2010).
[3] O. Bierwagen, Semiconductor Science and Technology (to be published).
[4] S. Lany and A. Zunger, Phys. Rev. Lett. **98**, 045501 (2007).
[5] P. Ágoston, P. Erhart, A. Klein, and K. Albe, J. Phys.: Condens. Matter **21**, 455801 (2009).
[6] P. King and T. D. Veal, J. Phys.: Condens. Matter **23**, 334214 (2011).
[7] S. Limpijumnong, P. Reunchan, A. Janotti, and C. G. Van de Walle, Phys. Rev. B **80**, 193202 (2009).
[8] O. Warschkow, L. Miljacic, D. Ellis, G. Gonzalez, and T. Mason, J. Am. Ceram. Soc. **89**, 616 (2006).
[9] O. Bierwagen and J. S. Speck, Phys. Status Solidi A **211**, 48 (2014).
[10] O. Bierwagen and J. S. Speck, Appl. Phys. Lett. **101**, 102107 (2012).
[11] S. Lany and A. Zunger, Phys. Rev. B **80**, 085202 (2009).
[12] J. B. Varley, A. Janotti, C. Franchini, and C. G. Van de Walle, Phys. Rev. B **85**, 081109 (2012).
[13] P. Ágoston, C. Körber, A. Klein, M. J. Puska, R. M. Nieminen, and K. Albe, J. Appl. Phys. **108**, 053511 (2010).
[14] P. Ágoston, K. Albe, R. M. Nieminen, and M. J. Puska, Phys. Rev. Lett. **103**, 245501 (2009).
[15] P. Reunchan, X. Zhou, S. Limpijumnong, A. Janotti, and C. G. Van de Walle, Current Applied Physics **11**, S296 (2011).
[16] F. Fuchs and F. Bechstedt, Phys. Rev. B **77**, 155107 (2008).
[17] G. Frank and H. Köstlin, Appl. Phys. A **27**, 197 (1982).
[18] G. B. Gonzalez, T. O. Mason, J. P. Quintana, O. Warschkow, D. E. Ellis, J.-H. Hwang, J. P. Hodges, and J. D. Jorgensen, J. Appl. Phys. **96**, 3912 (2004).
[19] F. Tuomisto and I. Makkonen, Rev. Mod. Phys. **85**, 1583 (2013).
[20] Z. Galazka, R. Uecker, K. Irmscher, D. Schulz, D. Klimm, M. Albrecht, M. Pietsch, S. Ganschow, A. Kwasniewski, and R. Fornari, J. Cryst. Growth **362**, 349 (2013).
[21] Z. Galazka, R. Uecker, and R. Fornari, J. Cryst. Growth **388**, 61 (2014).
[22] Z. Galazka, K. Irmscher, M. Pietsch, T. Schulz, R. Uecker, D. Klimm, and R. Fornari, Cryst. Eng. Comm. **15**, 2220 (2013).
[23] M. Albrecht, R. Schewski, K. Irmscher, Z. Galazka, T. Markurt, M. Naumann, T. Schulz, R. Uecker, R. Fornari, S. Meuret *et al.*, J. Appl. Phys. **115**, 053504 (2014).
[24] M. Bertolaccini and L. Zappa, Il Nuovo Cimento B Series 10 **52**, 487 (1967).
[25] P. R. Guagliardo, E. R. Vance, Z. Zhang, J. Davis, J. F. Williams, and S. N. Samarin, J. Am. Ceram. Soc. **95**, 1727 (2012).
[26] E. Korhonen, F. Tuomisto, O. Bierwagen, J. S. Speck, M. E. White, and Z. Galazka, AIP Conference Proceedings **1583**, 368 (2014).
[27] F. Tuomisto, V. Ranki, K. Saarinen, and D. C. Look, Phys. Rev. Lett. **91**, 205502 (2003).
[28] J. Oila, A. Kemppinen, A. Laakso, K. Saarinen, W. Egger, L. Liszkay, P. Sperr, H. Lu, and W. J. Schaff, Appl. Phys. Lett. **84**, 1486 (2004).
[29] C. Rauch, I. Makkonen, and F. Tuomisto, Phys. Rev. B **84**, 125201 (2011).
[30] I. Makkonen *et al.* (unpublished).
[31] C. Rauch, F. Tuomisto, A. Vilalta-Clemente, B. Lacroix, P. Ruterana, S. Kraeusel, B. Hourahine, and W. J. Schaff, Appl. Phys. Lett. **100**, 091907 (2012).
[32] K. M. Johansen, A. Zubiaga, I. Makkonen, F. Tuomisto, P. T. Neuvonen, K. E. Knutsen, E. V. Monakhov, A. Yu. Kuznetsov, and B. G. Svensson, Phys. Rev. B **83**, 245208 (2011).
[33] F. Reurings, F. Tuomisto, C. S. Gallinat, G. Koblmüller, and J. S. Speck, Appl. Phys. Lett. **97**, 251907 (2010).